INORGANIC CHEMISTRY
FRONTIERS

RESEARCH ARTICLE

View Article Online
View Journal | View Issue

Cite this: *Inorg. Chem. Front.*, 2023, **10**, 1338

Cesium manganese halide perovskite-analogue nanocrystals with highly efficient energy conversion for flexible multifunctional fibers†

Xiuqiang Duan,[a] Kun Nie, *[a,b] Xuyi Wang,[c] Chi-An Cheng,[d] Ranran Zhou,[a] Ziyao Hu,[a] Junbao Yan,[a] Lefu Mei,[e] Xiaoxue Ma,*[a] Songjun Yao,[a] Luoxin Wang[a] and Hua Wang*[a]

In recent years, all-inorganic perovskite materials have been considered and applied in various fields. In this work, we used an improved method to synthesize novel zero-dimensional (0D) lead-free $Cs_2Mn(Cl/Br)_4{\cdot}2H_2O$ perovskite-analogue nanocrystals (PA NCs) under aerobic conditions. At the same time, lead (Pb) was introduced into manganese (Mn) halide perovskite-analogue nanocrystals of $Cs_2Mn(Cl/Br)_4{\cdot}2H_2O$ *via* a hot-injection method. The PA NCs shows an intense orange light under a UV lamp. The fluorescence spectrum peak center of the PA NCs is located at around 598 nm, and the photoluminescence quantum yield (PLQY) is 41.12%. The PLQY of the original PA NCs was almost nonexistent at around 598 nm. The increase in PLQY was due to the replacement of Mn^{2+} with Pb^{2+}, which effectively promotes the transfer of excitation energy to Mn^{2+}. The Pb^{2+}-doped $Cs_2Mn(Cl/Br)_4{\cdot}2H_2O$ PA NCs also exhibit excellent stability and strong PL. We also applied the PA NCs to composite paper. The properties described in this study provide new design ideas and directions for potential optronic devices.

Received 25th November 2022,
Accepted 10th January 2023

DOI: 10.1039/d2qi02514k

rsc.li/frontiers-inorganic

Introduction

Since the hot-injection method was used to develop halide perovskites, there has been much interest in this area from researchers and scholars.[1–3] The photoelectric applications and research on various lead halide perovskites have advanced rapidly in recent years.[4–9] Lead halide perovskites are favored in the color changing field due to their unique color adjustability. However, the development of lead halide perovskites has been limited due to their harsh synthetic conditions and toxicity.[10] In terms of the development in this area, researchers have investigated using different metal elements to replace Pb^{2+} in order to obtain a perovskite structure similar to Pb^{2+}.[11] Some researchers have used Sn^{2+} and Ge^{2+} to replace Pb^{2+}.[12–14] However, Sn^{2+} and Ge^{2+} can be rapidly oxidized in air, so more stringent conditions are required to produce lead-free perovskites, but the perovskites obtained under such tough conditions show lower PL and stability compared to lead halide perovskites.

Manganese (Mn), as a transition metal element, is commonly used as a dopant to alter the optical properties and electrical properties of perovskite crystals.[15–18] Studies have shown that the introduction of Mn^{2+} into lead halide perovskites can improve the stability and optical properties of perovskites. Double peak emission occurs when Mn^{2+} is incorporated into $CsPbX_3$ (X = Cl, Br) crystals.[19–21] Mn^{2+} has the advantages of low toxicity and emits Mn^{2+} d–d transitions with a long energized state lifetime. Mn^{2+} has been thought to be an effective light emanation center in metal halide perovskites.[22] Moreover, extraordinary advances have been made in terms of the arrangement of manganese-based perovskites using Mn^{2+} instead of Pb^{2+}.[23–26] Mn^{2+} shows different properties in different coordination modes. It ordinarily exhibits green emission in tetrahedral coordination, but orange or red emission in six-coordinate octahedral mode.[27–29] The d–d transitions of Mn^{2+} decided by spin and parity selection rules are related to the content of Mn, and Mn–Mn coupling results in

[a]*School of Materials Science and Engineering, Hubei Key Laboratory for New Textile Materials and Applications and State Key Laboratory of New Textile Materials & Advanced Processing Technology, Wuhan Textile University, Wuhan 430200, P. R. China. E-mail: knie@wtu.edu.cn, maxiaoxue2010@126.com, huawangabc@163.com*
[b]*Key Laboratory of Testing and Tracing of Rare Earth Products for State Market Regulation, Jiangxi University of Science and Technology, Ganzhou 341000, P.R. China*
[c]*China Bluestar Chengrand Co., Ltd, High Tech Organic Fiber Key Laboratory of Sichuan Province, Chengdu 610042, China*
[d]*School of Pharmacy, Taiwan University, Taipei 100025, Taiwan, China*
[e]*Beijing Key Laboratory of Materials Utilization of Nonmetallic Minerals and Solid Wastes, National Laboratory of Mineral Materials, School of Materials Science and Technology, China University of Geosciences (Beijing), Beijing 100083, P. R. China*
† Electronic supplementary information (ESI) available. See DOI: https://doi.org/10.1039/d2qi02514k

low photoluminescence quantum yield (PLQY) at high content.[30,31] Dopants should thus be selected to lower the content of Mn^{2+}, and as the radius of Mn^{2+} is similar to that of Pb^{2+}, doping with Pb^{2+} is an excellent choice for ideally improving the optical properties of manganese-based perovskites.[17–21,32]

In this study, we successfully synthesized $Cs_2Mn(Cl/Br)_4{\cdot}2H_2O$ PA NCs and incorporated Pb into these PA NCs *via* hot injection. The replacement of lead improves the optical properties and stability of the PA NCs. We combined the PA NCs with composite paper to create a composite paper with color changing function. Also, the excellent optical properties mean that the resulting PA NCs can be used as a new photoelectric material. Finally, the PA NCs can be produced in an atmospheric environment, which opens up new possibilities for future optoelectronic applications.

Results and discussion

In this work, we synthesized $Cs_2Mn(Cl/Br)_4{\cdot}2H_2O$ perovskite-analogue nanocrystals (PA NCs) with a 0-dimensional (0D) octahedral structure, and Pb^{2+}-incorporated $Cs_2Mn(Cl/Br)_4{\cdot}2H_2O$ PA NCs *via* a hot-injection method. The spatial crystal structure of $Cs_2Mn(Cl/Br)_4{\cdot}2H_2O$ is projected along the *a*-axis, as illustrated in Fig. 1a.[34] $Cs_2Mn(Cl/Br)_4{\cdot}2H_2O$ and $CsMn(Cl/Br)_3{\cdot}2H_2O$ have similar spatial structures, and Mn^{2+} in $Cs_2Mn(Cl/Br)_4{\cdot}2H_2O$ and $CsMn(Cl/Br)_3{\cdot}2H_2O$ adopts the same six-coordinate structure.[35] The distinction is that the two water molecules in $CsMn(Cl/Br)_3{\cdot}2H_2O$ move from adjacent positions to inverse positions, forming the 0D structure $Cs_2Mn(Cl/Br)_4{\cdot}2H_2O$. The crystal structures of the original PA NCs and Pb^{2+}-doped PA NCs both contain octahedral $[Mn(Cl/Br)_4(OH)_2]^{4-}$.[30,35–37] After the introduction of Pb^{2+}, Mn^{2+} was replaced with Pb^{2+} to form a $[Pb(Cl/Br)_4(OH)_2]^{4-}$ octahedral structure. The preparation of the aramid chopped fibers/polyphenylene sulfide (ACFs/PPS) composite is detailed in the Experimental section. The specific steps for impregnating the composite paper with colloidal solution are shown in Fig. 1b. To determine the specific situation of Pb^{2+} incorporation, we recorded X-ray diffraction (XRD) measurements. Most of the peaks in the XRD patterns of the original PA NCs and Pb^{2+}-doped PA NCs, as shown in Fig. 2a, can be assigned to the parameters of $Cs_2MnCl_4{\cdot}2H_2O$ (PDF#21-0214) with a triclinic crystal structure. With an increase in Pb^{2+} content, the XRD pattern shows an extra diffraction peak in the PA NC sample. By comparison with standard cards, we discovered that the reaction generates a relatively small fraction of $Cs_2MnBr_4{\cdot}2H_2O$ (PDF#50-0630). We improved crystal purity by washing the crystals with hexane many times, it did not affect the final experimental results. If we continued to increase the lead content, there was more inclination towards the formation of a three-dimensional stable structured $CsPb(Cl/Br)_3$: Mn^{2+} perovskite (Fig. S1†) due to the lower bond energy of Pb–Cl/Br than that of Mn–X (X = Cl, Br or OH). We selected XRD data with a lower doping content (Mn : Pb = 1 : 0.05) for comparison, and the characteristic peaks in the 2θ region of 30°–32° can be designated to the (−112), (102), (200) and (120) crystal planes, as shown in Fig. 2b. As the ionic radius of Br is larger than that of Cl, resulting in lattice expansion, the diffraction peaks of $Cs_2Mn(Cl/Br)_4{\cdot}2H_2O$ shift to smaller angles than those of $Cs_2MnCl_4{\cdot}2H_2O$. Similarly, when a small amount of Pb^{2+} content (Mn : Pb = 1 : 0.05) was added to the $Cs_2Mn(Cl/Br)_4{\cdot}2H_2O$ PA NCs, as the ionic radius of Pb is larger than that of Mn the XRD peak moves monotonously to a smaller angle.

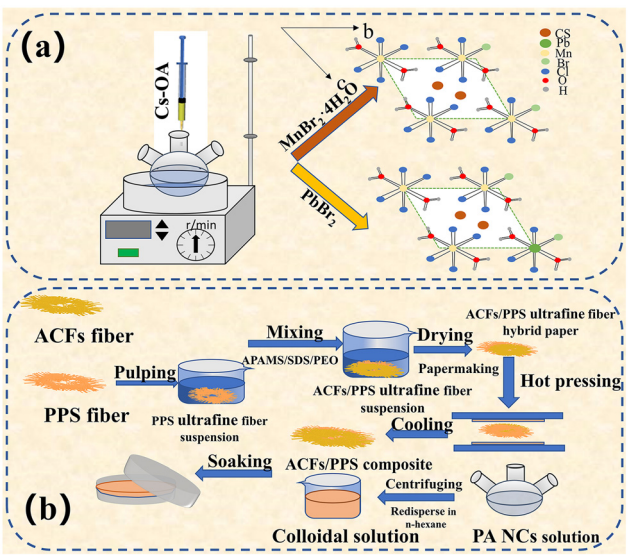

Fig. 1 (a) The spatial crystal structures of $Cs_2Mn(Cl/Br)_4{\cdot}2H_2O$ and $Cs_2Mn(Cl/Br)_4{\cdot}2H_2O{:}Pb^{2+}$ projected along the *a*-axis prepared *via* a hot-injection method. (b) Preparation process of an ACFs/PPS composite using a colloidal solution.

X-band electronic parameter resonance (EPR) spectra were used to investigate the surrounding of Mn^{2+} ions in the samples. As shown in Fig. 2c, all EPR spectra reveal background signals originating from the Mn^{2+} center, while samples lacking Pb^{2+}-incorporation show no evident 6-fold hyperfine splitting, indicating severe spin relaxation due to high Mn concentrations. Furthermore, the linewidth of Pb^{2+}-doped samples is larger than that of the original samples and the EPR signal intensity is weaker. In general, weak spin–spin coupling results in a wider and weaker EPR signal.[30,36] Thus, the magnetic exchange interaction between Mn^{2+} ions appears to be decreased by Pb^{2+} incorporation, indicating that Pb^{2+} ions were successfully incorporated.

Fig. 3a–f show SEM images of the pristine and Pb^{2+}-doped PA NCs. These PA NCs are block-like in appearance with an average diameter of approximately 100 nm. At the same time, we also found that with an increase in Pb^{2+} content, some blocks with relatively small diameters began to appear, until the proportion of the addition was Mn : Pb = 1 : 0.20, the average diameter of PA NCs generated in the same reaction time became much smaller (Fig. 3e). These PA NCs were nucleated quickly at high temperature, and their morphology was very poor due to them containing two water molecules.

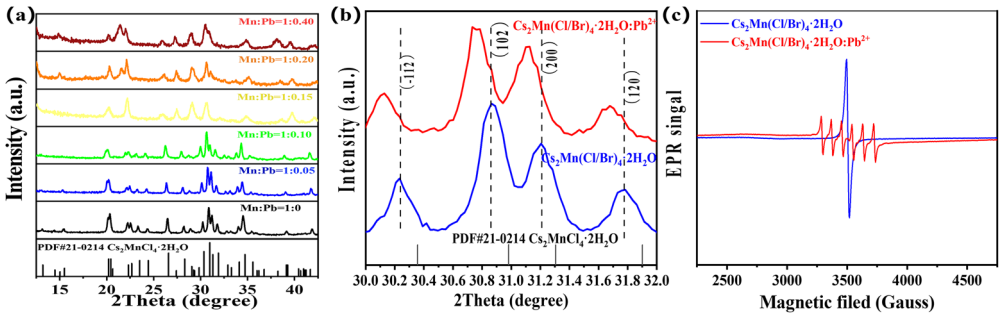

Fig. 2 (a) XRD patterns of the PA NCs. (b) Local broadened view of the crystal planes in the XRD patterns. (c) X-band EPR spectra of pristine and Pb^{2+}-doped PA NCs.

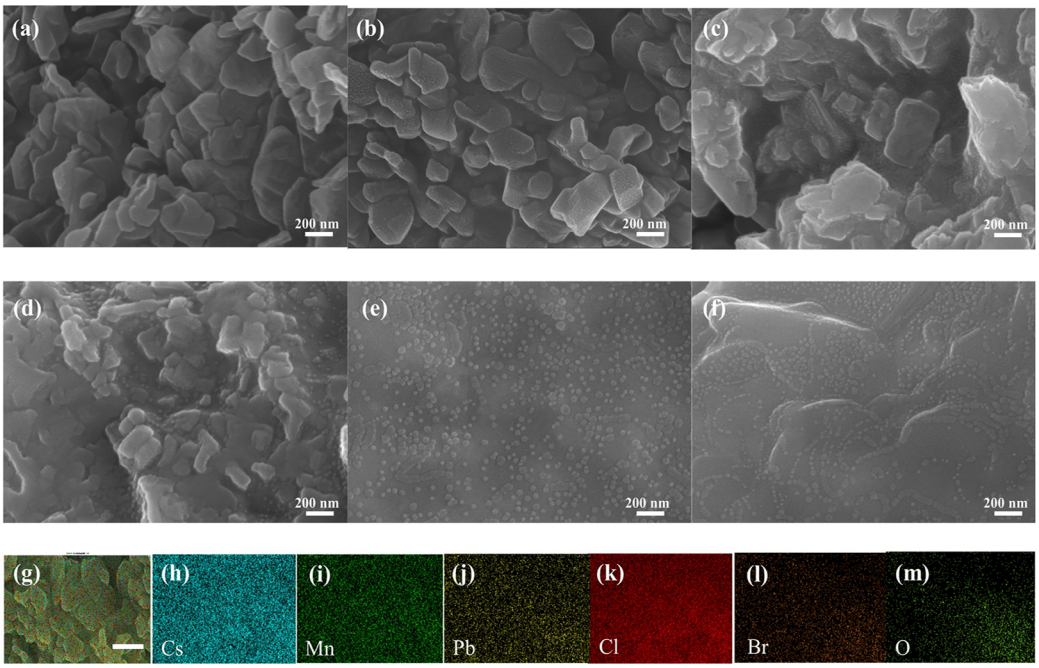

Fig. 3 SEM images of (a) pristine and Pb^{2+}-incorporated $Cs_2Mn(Cl/Br)_4{\cdot}2H_2O$ PA NCs. (b) Mn : Pb = 1 : 0.05. (c) Mn : Pb = 1 : 0.10. (d) Mn : Pb = 1 : 0.15. (e) Mn : Pb = 1 : 0.20. (f) Mn : Pb = 1 : 0.40. (g)–(m) EDS elemental mapping of $Cs_2Mn(Cl/Br)_4{\cdot}2H_2O$:$Pb^{2+}$ PA NCs (Mn : Pb = 1 : 0.05). Scale bar: 500 nm.

The incorporation of Pb^{2+} reduced the crystallization rate of the PA NCs.[30,35,38] The PA NCs with Pb^{2+} were more monodisperse than the original PA NCs. The energy-dispersive X-ray spectroscopy (EDS) images and relevant elemental mapping of the Pb^{2+}-doped sample (Mn : Pb = 1 : 0.05) illustrate uniform distributions of the Cs, Pb, Mn, Br, Cl, and O elements (Fig. 3g–m), which also confirms the successful preparation of the Pb^{2+}-doped PA NCs (see the details in the ESI, Fig. S2, S3 and Table S1†).

Afterward, we continued to explore the optical properties of the original $Cs_2Mn(Cl/Br)_4{\cdot}2H_2O$ PA NCs and $Cs_2Mn(Cl/Br)_4{\cdot}2H_2O$ PA NCs doped with different Pb^{2+} contents. We researched the UV–vis absorption and photoluminescence (PL) properties of the original and Pb^{2+}-incorporated samples, as shown in Fig. 4. Fig. 4a shows that the visible absorption spectra of the original sample and Pb^{2+}-doped sample are similar. The absorption at 520 nm is comparatively weak owing to the low spin band gap of octahedrally coordinated Mn, corresponding to a transition from $^6A_{1g}$ to $^4T_{1g}$.[29,35,36,39] With the addition of more Pb^{2+}, evident exciton absorption peaks were observed at 400 and 365, which may be due to the introduction of octahedral $[Pb(Cl/Br)_4(OH)_2]^{4-}$.[36] Furthermore, we also characterized these PA NCs by PL spectroscopy (Fig. 4b). The scan speed of the F-4700 spectrometer employed was 1200 nm min^{-1}, and the slit was 5 nm. It can be seen that the $Cs_2Mn(Cl/Br)_4{\cdot}2H_2O$ PA NCs exhibit no fluorescence peak in the range of 550 nm to 725 nm under the excitation of 365 nm. When doped with Pb^{2+}, there was a double peak emission at the excitation of 365 nm. The narrow band (blue band) occurring at 400 nm–450 nm is considered to be the intrinsic

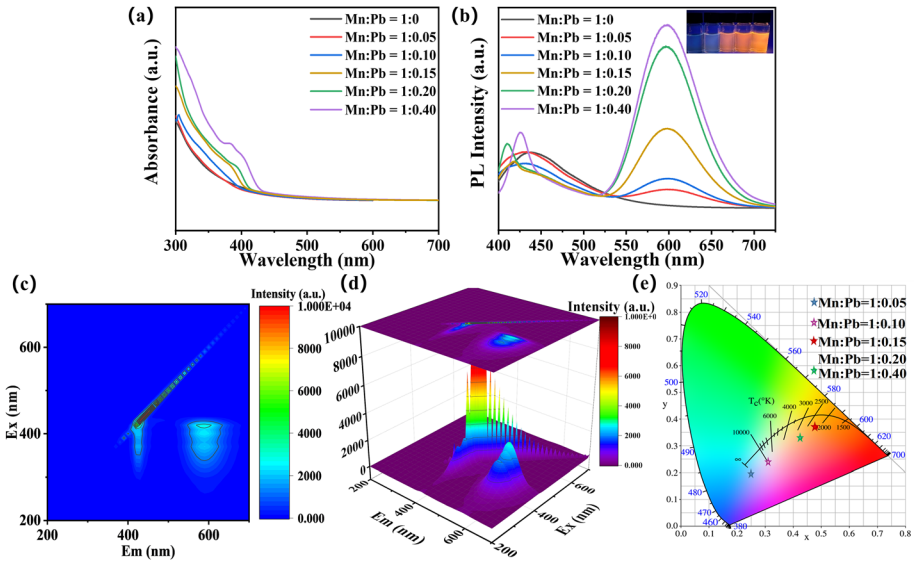

Fig. 4 (a) UV–vis absorbance of PA NCs. (b) PL spectra of pristine (λ_{ex} = 365 nm) and Pb^{2+}-doped $Cs_2Mn(Cl/Br)_4{\cdot}2H_2O$ PA NCs (λ_{ex} = 365 nm). (c) and (d) 2D and 3D fluorescence spectra of Pb^{2+}-incorporated $Cs_2Mn(Cl/Br)_4{\cdot}2H_2O$ PA NCs. (e) Color coordinates of Pb^{2+}-incorporated $Cs_2Mn(Cl/Br)_4{\cdot}2H_2O$ PA NCs, (inset: a photograph of the several Pb^{2+} doped samples under a 365 nm UV lamp).

exciton emission of $[MnX_6]^{4-}$ (X = Cl, Br, OH) when a low ratio of Pb^{2+} is incorporated,[37] which corresponds to the emission spectra. When the ratio of Pb^{2+} incorporated increases by a certain ratio (Mn : Pb = 1 : 0.15), the blue emission is designated to the intrinsic exciton emission of the lead halide unit $[PbX_6]^{4-}$ (X = Cl, Br, OH),[15–19] and the full width at half maximum (FWHM) of the blue emission peak also becomes smaller, which is consistent with the intrinsic emission of octahedral $[Pb(Cl/Br)_4(OH)_2]^{4-}$. This corresponds to the characteristic peak of the absorption of octahedral $[Pb(Cl/Br)_4(OH)_2]^{4-}$ at Mn : Pb = 1 : 0.15, and also corresponds to the different colors of light emitted under a 365 nm UV light. The blue peak was not fixed at 400–450 nm; its position was dependent on the ratio of doped Cl to Br.[16] The obvious red shifts for both the absorption edge and PL band (blue band) contributed to a reduction in the bandgap of Cl^- by Br^-. As the content of Pb^{2+} increased, the orange became brighter, indicating that octahedral $[Pb(Cl/Br)_4(OH)_2]^{4-}$ transfers most of its energy to octahedral $[Mn(Cl/Br)_4(OH)_2]^{4-}$ through intersystem crossing (ISC) from the light absorption of the blue-violet band. 3D scanning spectra of Pb^{2+} doped PA NCs are shown in Fig. 4c and d, which are consistent with our previous results. Fig. 4e shows the color coordinates of the Pb^{2+}-incorporated $Cs_2Mn(Cl/Br)_4{\cdot}2H_2O$ PA NCs under UV irradiation.

In addition, as a result of the original PA NCs exhibiting no fluorescence peak from 550 nm to 725 nm, we did not measure related PLQY and time-resolved photoluminescence (TRPL) spectra. We measured the PLQYs of the Pb^{2+}-incorporated $Cs_2Mn(Cl/Br)_4{\cdot}2H_2O$ PA NCs (Mn : Pb = 1 : 0.05, 1 : 0.10, 1 : 0.15, 1 : 0.20, 1 : 0.40). The absolute PLQYs of the Pb^{2+}-incorporated PA NCs at 598 nm were 2.84%, 7.31%, 26.14%, 33.53% and 41.12%, respectively (Fig. 5a). The PLQYs of the Pb^{2+}-doped PA NCs are shown in Fig. S4.† These data show that the PLQY was always significantly enhanced with an increase in Pb^{2+} content. If the quantum efficiency of the blue part was included, the PLQY reached more than 50%.[15–19,36] TRPL

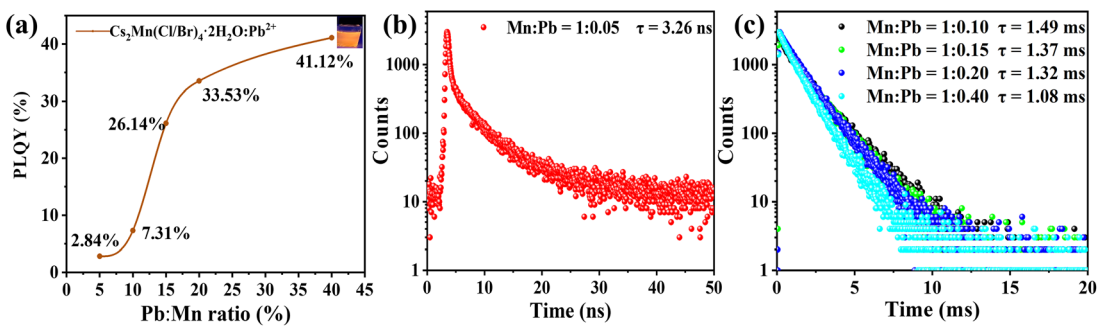

Fig. 5 (a) PLQY of Pb^{2+}-doped PA NCs at 598 nm, TRPL decay curves of Pb^{2+}-doped PA NCs revealed on logarithmic intensity scales at (b) Mn : Pb = 1 : 0.05 and (c) Mn : Pb = 1 : 0.10, 1 : 0.15, 1 : 0.20, 1 : 0.40.

measurements help to clarify the impact of the incorporation of the Pb^{2+} on the optical properties. The TRPL decay curves of Mn^{2+} emission were fitted using a double exponential (1):[36,40]

$$I(t) = A_1 \exp(-t/\tau_1) + A_2 \exp(-t/\tau_2). \quad (1)$$

The following eqn (2) was used to calculate the average lifetime:[33]

$$\tau_{avg} = (A_1{\tau_1}^2 + A_2{\tau_2}^2)/(A_1\tau_1 + A_2\tau_2). \quad (2)$$

Where A_1 and A_2 are the amplitudes and τ_1 and τ_2 represent the fast and slow decay lifetimes, respectively I and t are fluorescence intensity and time, respectively. The fitting parameters are listed in Table S2.† As shown in Fig. 5b, the average lifetime of Pb^{2+} at 598 nm was 3.26 ns when it was doped with a low Pb^{2+} content. For Mn^{2+} transitioning from $^4T_1$ to $^6A_1$, the typical lifetime is ordinarily between 1 and 10 ms, but the fluorescence lifetime of $Cs_2Mn(Cl/Br)_4{\cdot}2H_2O{:}Pb^{2+}$ (Mn : Pb = 1 : 0.05) is two orders of magnitude less, which is unusual. This ought to be attributed to the multiphonon decay resulting from the affiliation of phonons with the O–H stretching vibration mode of H_2O, resulting in a shortened lifetime.[35,38] While $Cs_2Mn(Cl/Br)_4{\cdot}2H_2O$ is a 0D structure, the H_2O separated from the octahedron leads to more severe quenching.[35,39] However, upon an increase in Pb^{2+} content (Fig. 5c), the average lifetime of the Pb^{2+}-doped PA NCs rises to more than 1 ms, which may be caused by a reduction in the coupling between Mn–Mn pairs. After the replacement of Mn^{2+} by Pb^{2+}, and its average lifetime was 1.08 ms in the PA NCs with the highest Pb^{2+} doping content, the lifetime showed a decreasing trend, which may be due to the quenching caused by the increased Pb^{2+}content.[35,36] Based on previous analysis, Fig. 6 shows the photophysical process in the Pb^{2+}-doped PA NCs. The Pb^{2+} in the $[PbX_6]^{4-}$ octahedral unit can break the magnetic coupling or symmetry between Mn^{2+} pairs, relax the rules of spin and parity selection,[29,30,38] and act as an effective UV absorber for exciton production. The Mn^{2+} in the $[MnX_6]^{4-}$ octahedral unit works as an effective energy acceptor *via* intersystem crossing (ISC), and thus improves the $^4T_{1g}$–$^6A_{1g}$ transition process caused by an increase in exciton density in $^4T_{1g}$, thereby improving the PLQY. By introducing $[PbX_6]^{4-}$ as the basic sensitizer, the low PLQY caused by the prohibited transition in the $Cs_2Mn(Cl/Br)_4{\cdot}2H_2O$ PA NCs was overcome.[29,38,39]

Meanwhile, we applied the PA NCs with fluorescence properties to ACF/PPS composite paper, as shown in Fig. 7a. We found that ACFs/PPS composite paper soaked in Pb^{2+}-doped PA NC solution showed strong orange light under a 365 nm UV lamp, making it of potential use in the anti-counterfeiting field. Fig. 7b shows the CIE chromaticity diagram illustrating

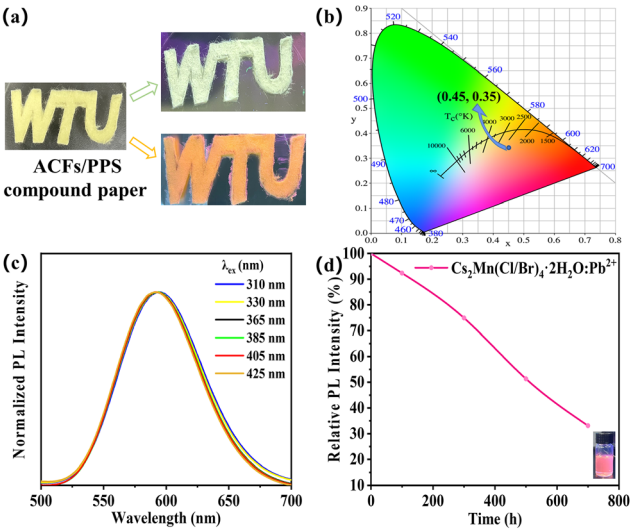

Fig. 7 (a) Patterned words images of Pb^{2+}-doped PA NCs (Mn : Pb = 1 : 0.40) under visible and UV light. (b) CIE chromaticity diagram for the composite paper. (c) Excitation-wavelength-dependent (310–425 nm) PL spectra of Pb^{2+}-doped PA NCs (Mn : Pb = 1 : 0.40). (d) Stability of Pb^{2+}-doped PA NCs (Mn : Pb = 1 : 0.40) determined to monitor the PL intensity of the solution as a function of hexane at 598 nm. Insets: sample under a 365 nm UV lamp after being dissolved in colloidal solution for one month.

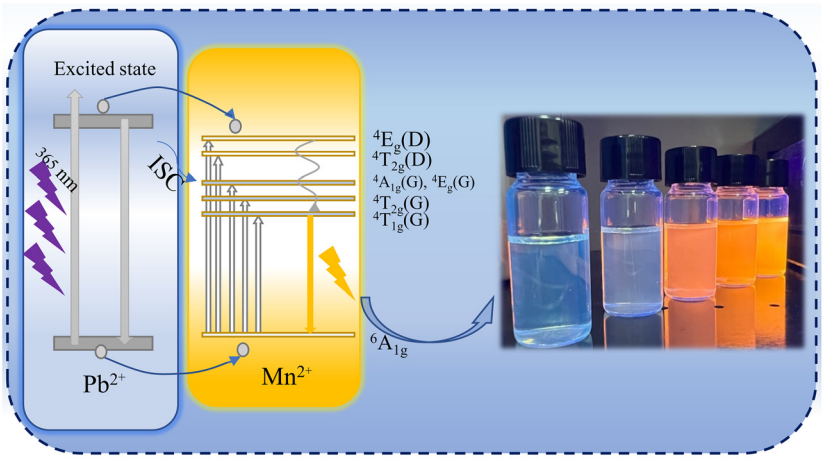

Fig. 6 Diagram of the light absorption, ISC (intersystem crossing) and PL processes of the Pb^{2+}-doped $Cs_2Mn(Cl/Br)_4{\cdot}2H_2O$ PA NCs.

the orange emission at (0.45, 0.35) of the composite paper. When the excitation wavelength changed from 310 nm to 425 nm, no changes were observed in the PL emission spectra, as shown in Fig. 7c. The autonomy of the PL emission spectra at excitation wavelength verifies that orange emission was caused by the relaxation of the same excited state.

To demonstrate the outstanding stability of the $Cs_2Mn(Cl/Br)_4{\cdot}2H_2O{:}Pb^{2+}$ PA NCs, we re-dispersed the centrifugally-precipitated material into 10 mL of *n*-hexane, 1 mL of OA, and 1 mL of OLA to form a colloidal solution, the fluorescence intensity of which was investigated at different time periods under aerobic conditions. Even after one month, the orange light emission at 598 nm still maintained a certain intensity, as shown in Fig. 7d. In order to apply composite paper in real-world scenarios, we tested the stability of the composite paper in different environments. As shown in Fig. 8a, the composite paper was placed in a freezer at −50 °C for 72 h, and we found that the composite paper still maintained 62% fluorescence performance, as shown in Fig. 8c. As can be seen in Fig. 8b, we exposed the composite paper to the sun to test the fluorescence performance of the composite paper at different time points. After being exposed to an outdoor temperature of 36 °C for 2 h, the composite paper still exhibited bright fluorescence performance under a UV lamp. During its exposure to the sun, we applied an infrared thermal imager to monitor the surface temperature of the composite paper, as shown in Fig. 8d. Then, we soaked the composite paper with water, and we observed that after soaking in water for 20 min, the composite paper still showed strong orange light under the UV lamp, as indicated in Fig. 8e. These stability experiments show that the composite paper can be well used in color-changing fibers. Due to its excellent luminescence characteristics and stability, this material can be used as a color conversion material for LEDs. As shown in Fig. 9a, the device shows bright orange light with color coordinates of (0.57, 0.37) (Fig. 9c), and the corresponding emission spectrum is shown in Fig. 9b. This LED device has the ability to remain unaltered for extended continuous operation time. In future work, we can also try to react it with APTES as a ligand to ensure that the PA NCs are preserved for a longer period of time.

Experimental section

Materials

Cesium carbonate (Cs_2CO_3, 99.99%), *n*-hexane (>99%, GC), oleylamine (OAm, 80–90%), 1-octadecene (ODE, >90%, GC), manganese(II) chloride ($MnCl_2$, 99%), lead(II) bromide ($PbBr_2$,

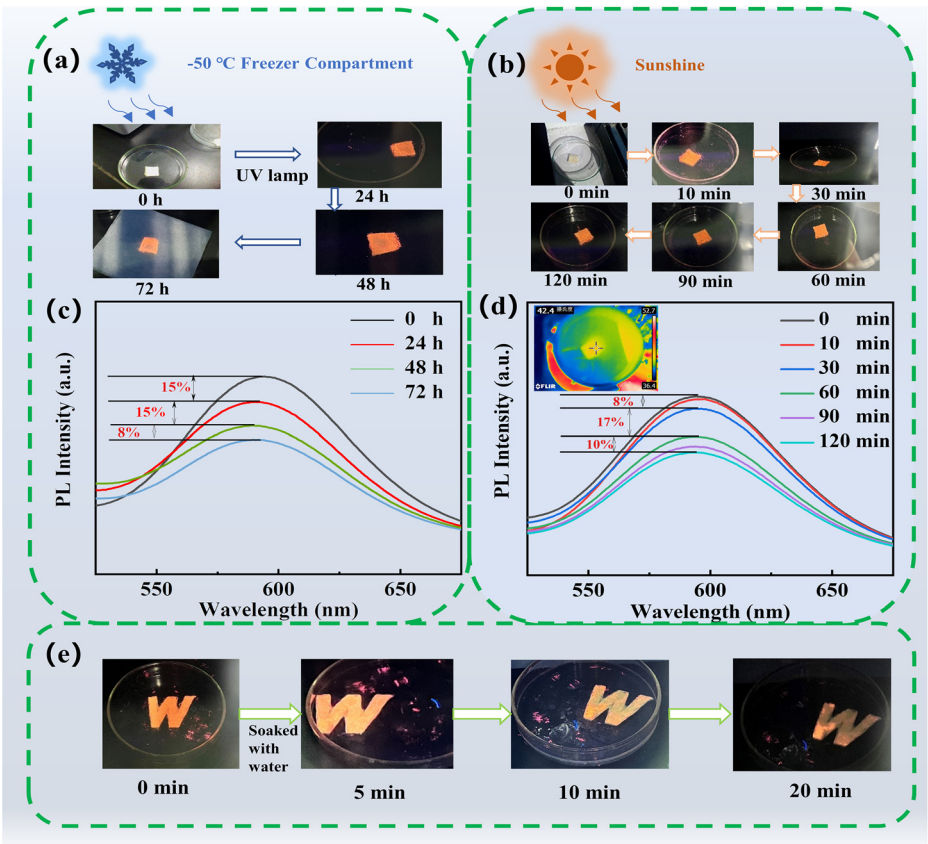

Fig. 8 (a) Stability testing of compound paper placed in a −50 °C refrigerator. (b) Compound paper placed in sunshine. (c) Fluorescence spectra of compound paper placed in a −50 °C refrigerator. (d) Fluorescence spectra of compound paper placed in sunshine. (e) Stability testing of compound paper soaked in water.

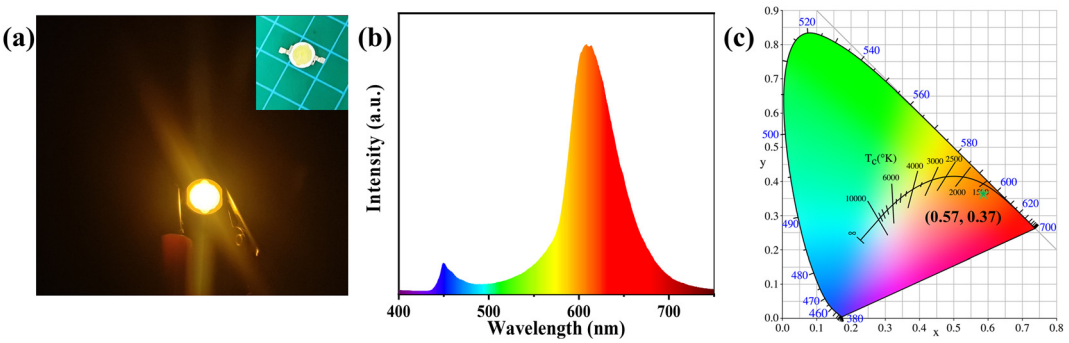

Fig. 9 (a) Fluorescence image. Inset: optical image of the LED. (b) PL emission spectrum. (c) CIE chromaticity coordinates of the LED from Pb^{2+}-doped PA NCs.

99.9%), oleic acid (OA, AR), and manganese(II) bromide tetrahydrate ($MnBr_2{\cdot}4H_2O$, 99%) were used in this work. All reagents were purchased from Aladdin Chemical Co., Ltd (Shanghai, China) and used directly without further purification. Ethyl acetate (EAC, AR) was purchased from Sinopharm. Aramid chopped fibers (ACFs) were supplied by China Bluestar Chengrand Chemical Research and Design Institute Co., Ltd, (China). Polyethylene oxide (PEO, $M_w = 2 \times 10^6$) was purchased from Sumitomo Keiretsu Co., Ltd, Japan. Anionic polyacrylamide (APAM, $M_w = 3 \times 10^6$), acetone and sodium dodecylbenzene sulfonate (SDS) were purchased from China Pharmaceutical Group Chemical Reagent Co., Ltd. Silicone defoamer was provided by China's Lusen Chemical Co., Ltd.

Preparation of cesium oleate precursors. Cesium oleate solution was prepared according to the approach detailed by Protesescu *et al.*[33] Briefly, 0.203 g of Cs_2CO_3, 0.6 mL of OA, and 7.5 mL of ODE were added to a three-neck flask and heated to 120 °C for 30 min, and then heated to 150 °C until all the Cs_2CO_3 had reacted with OA. The solution turned to a pale yellow. The resulting Cs–OA solution was stored and preheated to 150 °C before use.

Preparation of the $Cs_2Mn(Cl/Br)_4{\cdot}2H_2O$ PA NCs. 0.1183 g of $MnCl_2$, 0.027 g of $MnBr_2{\cdot}4H_2O$, 25 mL of ODE, 2.5 mL of OAm and 2.5 mL of OA were reacted in a three-necked flask for 1 h at 120 °C to completely dissolve $MnCl_2$ and $MnBr_2{\cdot}4H_2O$. The color of the solution changed from black to pale yellow and finally brown. After the temperature was raised to 145–150 °C, the temperature was left to stabilize for a while, before 2 mL of hot 150 °C Cs–oleate solution was rapidly added into the reaction solution, and the reaction blend was cooled using a water bath.

Preparation of Pb^{2+}-doped $Cs_2Mn(Cl/Br)_4{\cdot}2H_2O$ PA NCs. $MnCl_2$ and $PbBr_2$ in a specific molar ratio (1 : 0.05, 1 : 0.10, 1 : 0.15, 1 : 0.20 and 1 : 0.40) were mixed with 25 mL of ODE, 2.5 mL of OAm and 2.5 mL of OA in a three-neck flask for 1 h at 120 °C. After $MnCl_2$ and $PbBr_2$ were used up, the temperature was increased to 145–150 °C, and in the same way as above, 2 mL of hot 150 °C Cs–oleate solution was quickly infused, and the reaction blend was cooled using a water bath.

Purification. The $Cs_2Mn(Cl/Br)_4{\cdot}2H_2O$ PA NCs and $Cs_2Mn(Cl/Br)_4{\cdot}2H_2O$:$Pb^{2+}$ PA NCs were extricated from the unrefined solution by centrifuging at 10 000 rpm for 5 min to the supernatant containing unreacted precursor and by products was disposed. After that, 5 mL of *n*-hexane was added to the precipitation for dispersion, and then 5 mL of ethyl acetate was also added to induce aggregation. The solution was centrifuged at 10 000 rpm for 5 min. After centrifugation, the supernatant was discarded and the precipitates were redispersed in *n*-hexane to form a steady colloidal solution, with some of the precipitate taken and placed in an oven for drying before its subsequent characterization.

Preparation of the ACF/PPS compound paper. To remove impurities, the ACF and PPS microfiber non-woven fabrics were first cleaned with acetone. PPS ultrafine fiber pulp was created by beating PPS non-woven fabric in a valley-type beating machine. Then, in a mass ratio of 1 : 3 : 6, APAM, SDS, and PEO were added to deionized water and stirred at room temperature for 4 h to obtain a uniformly dispersed solution (APAMS/SDS/PEO). Following that, a fiber dissociator was used to disperse the dispersion of a PPS ultrafine fiber pulp and ACFs in a mass ratio of 3 : 7. A mixed fiber suspension was formed after the fibers were evenly distributed and completely dispersed in the dispersion. Finally, to obtain ACF/PPS hybrid papers, the hybrid fiber suspension was used in wet papermaking directly on a paper sheet forming machine.

Fabrication of LED from Pb^{2+}-doped $Cs_2Mn(Cl/Br)_4{\cdot}2H_2O$ PA NCs. Commercially available GaN light emitting diode (LED) chips without a phosphor coating were purchased from U King Optoelectronic Technology Inc. The GaN LED chip emission center was 380–385 nm, the operating voltage was 3.4 V. The Pb^{2+}-doped PA NCs powder was ground and mixed with *n*-hexane and repeatedly applied to the fluorescent coating, which was then dried in a vacuum oven and finally assembled into an LED.

Characterization. The photoluminescence spectra of the PA NCs were measured using a Hitachi fluorescence spectrophotometer F-4700 employing a xenon lamp as the excitation source at room temperature. The UV–vis absorption spectra of PA NCs were recorded using a A590 double beam scanning UV/vis spectrophotometer. An Edinburgh steady/transient fluorescence spectrometer FLS1000 was used for testing the decay of the photoluminescence and photoluminescence quantum

yield (PLQY). Scanning electron microscope (SEM) observations with energy-dispersive X-ray spectroscopy (EDS) analyses of the samples were carried out using a TESCAN MIRA LMS/TESCAN MIRA4 (Czech Republic) microscope. X-ray diffraction (XRD) patterns were measured on a PANalytical Empyrean powder X-ray diffractometer with monochromatic Cu Ka radiation, operated at 40 kV and 40 mA. Paramagnetic resonance spectra (ESR/EPR) were recorded using a Bruker EMX PLUS spectrometer at room temperature under a 365 nm lamp. A camera-obscura ultraviolet analyzer (ZF-7N) was used to observe fluorescence effects. A Yossen hand-held professional-grade thermal imager was used for thermal imaging.

Conclusion

In this study, 0D $Cs_2Mn(Cl/Br)_4{\cdot}2H_2O{:}Pb^{2+}$ PA NCs were synthesized *via* a simple hot-injection strategy. These PA NCs exhibit strong fluorescence performance, and their emission center is about 598 nm, with a PLQY of 41.12%. With the incorporation of Pb^{2+}, Pb exists as octahedral $[Pb(Cl/Br)_4(OH)_2]^{4-}$, playing an important role in transferring energy to Mn^{2+} and increasing light absorption in the blue-violet band, and decreasing magnetic coupling between Mn^{2+} pairs. These excellent properties significantly enhance the PLQY and stability of the $Cs_2Mn(Cl/Br)_4{\cdot}2H_2O{:}Pb^{2+}$ PA NCs. We applied a ACFs/PPS composite paper soaked in Pb^{2+}-doped PA NCs solution, which showed great stability in different environments, meaning that the composite paper can be used in color-changing fibers. Moreover, the Pb^{2+}-doped PA NCs also exhibit excellent properties in the field of luminescence. Finally, these PA NCs synthesized in air are expected to be a good choice for the mass production of optoelectronic devices in the future.

Author contributions

Kun Nie, Xiuqiang Duan, and Hua Wang conceived the concept and idea of the present paper, worked on the study design strategy, and selected the topics to be discussed. Xiuqiang Duan completed the main experiment and paper writing. Kun Nie, Xiaoxue Ma, and Hua Wang were responsible for guidance and supervision work, and at the same time, guided and revised the final paper writing. Xuyi Wang and Chi-An Cheng provided writing assistance and article revisions. Ziyao Hu and Ranran Zhou conducted literature searches, and abstracted the data from the eligible full text articles. Junbao Yan and Songjun Yao provided experimental guidance and experimental tests. Luoxin Wang and Lefu Mei supervised the study. All of the authors discussed the results and commented on the manuscript.

Conflicts of interest

There are no conflicts to declare.

Acknowledgements

This research was supported by the Key Laboratory of Testing and Tracing of Rare Earth Products for State Market Regulation (Jiangxi University of Science and Technology) (TTREP2022YB04), the National Natural Science Foundation of China (51872269, 52274273), the Science and Technology Research Project of Hubei Provincial Department of Education (B2021091), the Hubei Key Laboratory for New Textile Materials and Applications (Wuhan Textile University) (FZXCL202107), and the Open Project Program of High-Tech Organic Fibers Key Laboratory of Sichuan Province. The authors would like to thank Liu Nian and Liu Tianying from Shiyanjia Lab (**https://www.shiyanjia.com**) for the SEM characterizations.

References

1 D. Zhang, S. W. Eaton, Y. Yu, L. Dou and P. Yang, Solution-phase synthesis of cesium lead halide perovskite nanowires, *J. Am. Chem. Soc.*, 2015, **137**, 9230–9233.
2 D. Nasipuri, A. Patra, S. Bera, S. K. Dutta and N. Pradhan, Nucleophile-controlled halide release from the substitution reaction of haloketone for facet tuning and manganese doping in $CsPbCl_3$ nanocrystals, *J. Phys. Chem. Lett.*, 2022, **13**, 4506–4512.
3 Y. Bekenstein, B. A. Koscher, S. W. Eaton, P. Yang and A. P. Alivisatos, Highly luminescent colloidal nanoplates of perovskite cesium lead halide and their oriented assemblies, *J. Am. Chem. Soc.*, 2015, **137**, 16008–16011.
4 R. Gong, F. Wang, J. Cheng, Z. Wang, Y. Lu, J. Wang and H. Wang, Weak-solvent-modulated optical encryption based on perovskite nanocrystals/polymer composites, *Chem. Eng. J.*, 2022, **446**, 137212.
5 S. J. Yoon, S. Draguta, J. S. Manser, O. Sharia, W. F. Schneider, M. Kuno and P. V. Kamat, Tracking iodide and bromide ion segregation in mixed halide lead perovskites during photoirradiation, *ACS Energy Lett.*, 2016, **1**, 290–296.
6 H. L. Wu, L. J. Yao, W. Q. Cao, Y. Yang, Y. J. Cui, D. R. Yang and G. D. Qian, Stable and wide-wavelength tunable luminescence of $CsPbX_3$ nanocrystals encapsulated in metal-organic frameworks, *J. Mater. Chem. C*, 2022, **10**, 5550–5558.
7 T. Chen, Y. Q. Xu, Z. X. Xie, W. H. Jiang, L. J. Wang and W. Jiang, Ionic liquid assisted preparation and modulation of the photoluminescence kinetics for highly efficient $CsPbX_3$ nanocrystals with improved stability, *Nanoscale*, 2020, **12**, 9569–9580.
8 D. A. Penares, J. N. Arenas, R. I. Alarcón, R. Abargues, J. P. M. Pastor and J. F. Royo, Enhanced optical response of InSe nanosheet devices decorated with $CsPbX_3$ (X=I, Br) perovskite nanocrystals, *Appl. Surf. Sci.*, 2021, **536**, 147939.
9 X. F. Wu, S. T. Hu, H. Shao, L. F. Li, W. D. Chen, B. Dong, L. Xu, W. Xu, D. L. Zhou, Z. N. Wu, H. W. Song and X. Bai,

Introducing ytterbium acetate to luminescent $CsPbCl_3$ nanocrystals for enhanced sensitivity of Cu^{2+} detection, *Inorg. Chem. Front.*, 2022, **9**, 44–50.

10 Y. Zhou, J. Chen, O. M. Bakr and H. T. Sun, Metal-doped lead halide perovskites: synthesis, properties, and optoelectronic applications, *Chem. Mater.*, 2018, **30**, 6589–6613.

11 Q. Q. Fan, G. V. McGee, J. Z. Ma, Q. N. Xu, S. Pan, J. Peng and Z. Q. Lin, Lead-free halide perovskite nanocrystals: crystal structures, synthesis, stabilities, and optical properties, *Angew. Chem., Int. Ed.*, 2020, **59**, 1030–1046.

12 J. Chen, Z. Y. Luo, Y. P. Fu, X. X. Wang, K. J. Czech, S. H. Shen, L. J. Guo, J. C. Wright, A. L. Pan and S. Jin, Tin (IV)-tolerant vapor-phase growth and photophysical properties of aligned cesium tin halide perovskite ($CsSnX_3$; X=Br, I) nanowires, *ACS Energy Lett.*, 2019, **4**, 1045–1052.

13 S. Yalameha, P. Saeidi, Z. Nourbakhsh, A. Vaez and A. Ramazani, Insight into the topological phase and elastic properties of halide perovskites $CsSnX_3$ (X=I, Br, Cl) under hydrostatic pressures, *J. Appl. Phys.*, 2020, **127**, 085102.

14 Z. Song, J. Zhao and Q. L. Liu, Luminescent perovskites: recent advances in theory and experiments, *Inorg. Chem. Front.*, 2019, **6**, 2969–3011.

15 D. Rossi, D. Parobek, Y. Dong and D. H. Son, Dynamics of exciton-Mn energy transfer in Mn-doped $CsPbCl_3$ perovskite nanocrystals, *J. Phys. Chem. C*, 2017, **121**, 17143–17149.

16 D. Parobek, B. J. Roman, Y. J. Dong, H. Jin, E. Lee, M. Sheldon and D. H. Son, Exciton-to-dopant energy transfer in Mn-doped cesium lead halide perovskite nanocrystals, *Nano Lett.*, 2016, **16**, 7376–7380.

17 Q. Wei, M. J. Li, Z. P. Zhang, J. Guo, G. C. Xing, T. C. Sum and W. Huang, Efficient recycling of trapped energies for dual-emission in Mn-doped perovskite nanocrystals, *Nano Energy*, 2018, **51**, 704–710.

18 D. Parobek, Y. T. Dong, T. Qiao and D. H. Son, Direct hot-injection synthesis of Mn-doped $CsPbBr_3$ nanocrystals, *Chem. Mater.*, 2018, **30**, 2939–2944.

19 K. Y. Xu, J. F. Vliem and A. Meijerink, Long-lived dark exciton emission in Mn-doped $CsPbCl_3$ perovskite nanocrystals, *J. Phys. Chem. C*, 2019, **123**, 979–984.

20 Z. Cao, J. Li, L. Wang, K. Xing, X. Yuan, J. L. Zhao, X. Gao and H. B. Li, Enhancing luminescence of intrinsic and Mn doped $CsPbCl_3$ perovskite nanocrystals through Co^{2+} doping, *Mater. Res. Bull.*, 2020, **121**, 110608.

21 Y. Zhou, C. Liu, Z. Y. Zhao, W. C. Zhang, K. Li, Y. Ye, C. F. Zhu and X. G. Meng, Enhanced luminescence of Mn doped $CsPbCl_3$ and CsPb(Cl/Br)3 perovskite nanocrystals stabilized in glasses, *J. Alloys Compd.*, 2020, **827**, 154349.

22 S. Y. Wang, X. X. Han, T. T. Kou, Y. Y. Zhou, Y. Liang, Z. X. Wu, J. L. Huang, T. Chang, C. Y. Peng, Q. L. Wei and B. S. Zou, Lead-free Mn II-based red-emitting hybrid halide $(CH_6N_3)_2MnCl_4$ toward high performance warm WLEDs, *J. Mater. Chem. C*, 2021, **9**, 4895–4902.

23 Z. J. Zhou, X. W. Liu, B. Zhao, H. Z. Shao, Y. S. Xu and M. H. Xu, Elemental mercury oxidation over manganese-based perovskite-type catalyst at low temperature, *Chem. Eng. J.*, 2016, **288**, 701–710.

24 S. Y. Yan, W. L. Tian, H. Chen, K. X. Tang, T. T. Lin, G. Y. Zhong, L. Z. Qiu, X. Y. Pan and W. Z. Wang, Synthesis of 0D manganese-based organic-inorganic hybrid perovskite and its application in lead-free red light-emitting diode, *Adv. Funct. Mater.*, 2021, **31**, 2100855.

25 H. X. Wei, Y. D. Huang, L. B. Tang, C. Yan, Z. J. He, J. Mao, K. H. Dai, X. W. Wu, J. B. Jian and J. C. Zheng, Lithium-rich manganese-based cathode materials with highly stable lattice and surface enabled by perovskite-type phase-compatible layer, *Nano Energy*, 2021, **88**, 106288.

26 C. R. Raja, S. Suresh, R. R. Bhavsar, V. K. Singh, A. S. Reddy and A. Upadhyay, Manganese-based layered perovskite solid-solid phase change material: synthesis, characterization and thermal stability study, *Mech. Mater.*, 2019, **135**, 88–97.

27 Q. Zhou, L. Dolgov, A. M. Srivastava, L. Zhou, Z. L. Wang, J. Shi, M. D. Dramićanin, M. G. Brik and M. M. Wu, Mn^{2+} and Mn^{4+} red phosphors: synthesis, luminescence and applications in WLEDs, A review, *J. Mater. Chem. C*, 2018, **6**, 2652–2671.

28 D. W. Liu, Q. H. Li, Z. Zhang and K. C. Wu, Stable lead-free Te-based double perovskites with tunable band gaps: a first-principles study, *New J. Chem.*, 2019, **43**, 14892–14897.

29 J. H. Wei, J. F. Liao, X. D. Wang, L. Zhou, Y. Jiang and D. B. Kuang, All-inorganic lead-free heterometallic $Cs_4MnBi_2Cl_{12}$ perovskite single crystal with highly efficient orange emission, *Matter*, 2020, **3**, 892–903.

30 X. L. Zhu, S. Q. Meng, Y. F. Zhao, S. Zhang, J. Zhang, C. L. Yin and S. Ye, Mn^{2+}-Mn^{2+} magnetic coupling effect on photoluminescence revealed by photomagnetism in $CsMnCl_3$, *J. Phys. Chem. Lett.*, 2020, **11**, 9587–9595.

31 M. N. Liu, H. A. Löytty, A. Hiltunen, E. Sarlin, S. Qudsia, J. H. Smått, M. Valden and P. Vivo, Manganese doping promotes the synthesis of bismuth-based perovskite nanocrystals while tuning their band structures, *Small*, 2021, **17**, 2100101.

32 M. Righetto, D. Meggiolaro, A. Rizzo, R. Sorrentino, Z. He, G. Meneghesso, T. C. Suma, T. Gatti and F. Lamberti, Coupling halide perovskites with different materials: From doping to nanocomposites, beyond photovoltaics, *Prog. Mater. Sci.*, 2020, **110**, 100639.

33 L. Protesescu, S. Yakunin, M. I. Bodnarchuk, F. Krieg, R. Caputo, C. H. Hendon, R. X. Yang, A. Walsh and M. V. Kovalenko, Nanocrystals of cesium lead halide perovskites ($CsPbX_3$, X=Cl, Br, and I): novel optoelectronic materials showing bright emission with wide color gamut, *Nano Lett.*, 2015, **15**, 3692–3696.

34 C. Heo and A. R. Lim, ^{133}Cs nuclear magnetic resonance relaxation study of the phase transition of $Cs_2MnCl_4{\cdot}2H_2O$ single crystals, *J. Korean Magn. Reson. Soc.*, 2010, **14**, 76–87.

35 H. Xiao, P. P. Dang, X. H. Yun, G. G. Li, Y. Wei, X. Xiao, Y. J. Zhao, M. S. Molokeev, Z. Y. Cheng and J. Lin, Solvatochromic photoluminescent effects in all-inorganic manganese(II)-based perovskites by highly selective solvent-induced crystal-to-crystal phase transformation, *Angew. Chem., Int. Ed.*, 2021, **60**, 3699–3707.

36 Q. Meng, L. Y. Zhou, Q. Pang, X. L. He, T. Y. Wei and J. Z. Zhang, Enhanced photoluminescence of all-inorganic manganese halide perovskite-analogue nanocrystals by lead ion incorporation, *J. Phys. Chem. Lett.*, 2021, **12**, 10204–10211.

37 Q. K. Kong, B. Yang, J. S. Chen, R. L. Zhang, S. P. Liu, D. Y. Zheng, H. L. Zhang, Q. T. Liu, Y. Y. Wang and K. L. Han, Phase engineering of cesium manganese bromides nanocrystals with color-tunable emission, *Angew. Chem., Int. Ed.*, 2021, **60**, 19653–19659.

38 W. Jia, R. Brundage and R. B. Yen, Isotope effects in the multiphonon relaxation of hydrated and deuterated cesium chloromanganate ($CsMnCl_3{\cdot}2H_2O$, $2D_2O$), *Phys. Rev. B: Condens. Matter Mater. Phys.*, 1983, **27**, 41–45.

39 B. Vargas, D. T. Reyes-Castillo, E. Coutino-Gonzalez, C. Sánchez-Aké, C. Ramos, C. Falcony and D. Solis-Ibarra, Enhanced luminescence and mechanistic studies on layered double-perovskite phosphors: $Cs_4Cd_{1-x}Mn_xBi_2Cl_{12}$, *Chem. Mater.*, 2020, **32**, 9307–9315.

40 R. R. Zhou, C. A. Cheng, S. Y. Qiu, J. Y. Chen, K. Nie, M. Y. Wu, P. L. Lin, H. Wang, L. X. Wang and L. F. Mei, A novel and facile synthesis strategy for highly stable cesium lead halide nanowire, *RSC Adv.*, 2021, **11**, 28716–28772.